Spin-Wave Diode and Circulator Based on Unidirectional Coupling

Krzysztof Szulc,[1,*] Piotr Graczyk,[2] Michał Mruczkiewicz,[3,4] Gianluca Gubbiotti,[5] and Maciej Krawczyk[1,†]

[1] *Faculty of Physics, Adam Mickiewicz University, Poznań, Uniwersytetu Poznańskiego 2, Poznań 61-614, Poland*
[2] *Institute of Molecular Physics, Polish Academy of Sciences, M. Smoluchowskiego 17, Poznań 60-179, Poland*
[3] *Institute of Electrical Engineering, SAS, Bratislava 841 04, Slovakia*
[4] *Centre for Advanced Materials Application CEMEA, Slovak Academy of Sciences, Dúbravská cesta 5807/9, Bratislava 845 11, Slovakia*
[5] *Istituto Officina dei Materiali del CNR (CNR-IOM), Sede Secondaria di Perugia, c/o Dipartimento di Fisica e Geologia, Università di Perugia, Perugia I-06123, Italy*

(Received 20 November 2019; revised 20 June 2020; accepted 18 August 2020; published 25 September 2020)

In magnonics, a fast-growing branch of wave physics characterized by low energy consumption, it is highly desirable to create circuit elements useful for wave computing. However, it is crucial to reach the nanoscale so as to be competitive with the electronics, which vastly dominates in computing devices. Here, based on numerical simulations, we demonstrate the functionality of the spin-wave diode and the circulator to steer and manipulate spin waves over a wide range of frequency in the GHz regime. They take advantage of the unidirectional magnetostatic coupling induced by the interfacial Dzyaloshinskii-Moriya interaction, allowing the transfer of the spin wave between thin ferromagnetic layers in only one direction of propagation. Using the multilayered structure consisting of Py and Co in direct contact with heavy metal, we obtain submicrometer-size nonreciprocal devices of high efficiency. Thus, our work contributes to the emerging branch of energy-efficient magnonic logic devices, giving rise to the possibility of application as a signal-processing unit in the digital and analog nanoscaled spin-wave circuits.

DOI: 10.1103/PhysRevApplied.14.034063

I. INTRODUCTION

A diode and a circulator are electronic and microwave components, which have found wide applications in many devices for signal processing. A diode allows the flow of signal in only one direction, and for microwaves, it is also known as an isolator. It already has equivalents in optics [1], heat transfer [2,3], acoustics [4,5], and spin Seebeck effect [6]. Diodes for spin waves (SWs) relying on the dipolar [7–9] or interfacial Dzyaloshinskii-Moriya interaction (IDMI) [10] were recently proposed. In circulators, the signal going from one port is always directed only to the nearest port, according to the same sense of rotation. It usually consists of three or four ports. Apart from microwaves and photonics, where the circulators have found applications [11–14], they have been recently demonstrated also for acoustic waves [15], while a demonstration for SWs is still missing. Circulators used in industry are mostly macroscopic devices. Their miniaturization with the possibility of implementation to real-life systems is a crucial point of the present studies.

Antisymmetric exchange interaction was described by Dzyaloshinsky [16] and Moriya [17] about 60 years ago. Recently, it has found interest due to induced chirality of the magnetization configuration [18,19] and nonreciprocity in the SW propagation [20–25]. The DMI can exist in bulk noncentrosymmetric crystals [26] or at the interface between ferromagnetic and heavy-metal layers (IDMI). The IDMI is of high interest due to a larger DMI constant value [27,28], flexibility in shaping its strength, and the possibility of working at the nanoscale.

In this paper, we propose a layered sequence of ultrathin ferromagnetic films where the presence of IDMI over one layer leads to asymmetric or even unidirectional coupling of SWs between the layers. Interestingly, the multilayer composition can work as a SW diode or a three- or four-port SW circulator, in dependence on the particular structurization. The proposed SW diode, based on Py ($Ni_{80}Fe_{20}$) and Co ultrathin films, offers isolation of SW signal in the reverse direction reaching 22 dB with respect to the transmission in the forward direction. From the application point of view, the functionality of the device is preserved for a broad GHz-frequency range. We investigate the coupling between SWs in a heterogeneous ultrathin bilayer by numerical frequency-domain and time-dependent simulations. Then we discuss the coupling strength and the

*krzysztof.szulc@amu.edu.pl
†krawczyk@amu.edu.pl

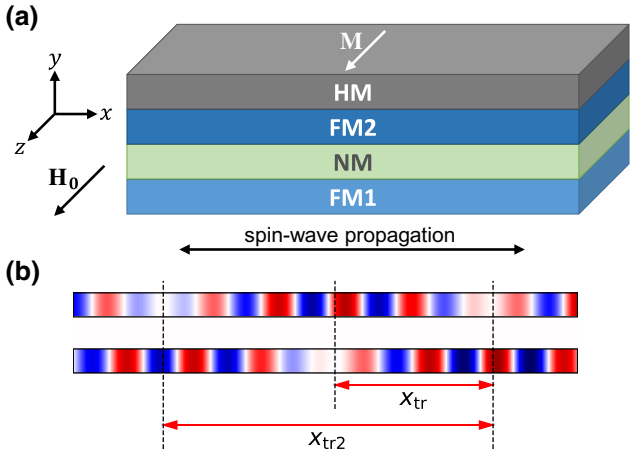

FIG. 1. (a) Schematic representation of the multilayer stack and the geometry considered. The layer sequence consists of two ferromagnetic films, FM1 and FM2, separated by the nonmagnetic layer (NM). In FM2, the IDMI is induced by the proximity with the heavy metal (HM). Generally, this structure underlies the unidirectional coupling in a wide range of frequency. (b) Definition of the transmission lengths x_{tr} and x_{tr2} on the basis of the SW in the coupled FM bilayer system.

SW transmission between the layers in the framework of the coupled-mode theory. Finally, we present possible realizations of the SW devices—the SW diode and the four-port circulator, with in-depth analysis of their efficiency.

The considered multilayer stack consists of two ferromagnetic (FM) layers separated by a nonmagnetic spacer, and heavy-metal layer in contact with one of the FM layers [Fig. 1(a)]. We consider SW propagation in the Damon-Eshbach geometry, where the magnetization M and the external magnetic field H_0 are aligned in plane of the films and perpendicular to SW propagation defined by the wavevector **k**.

II. THEORETICAL MODEL

Magnetization dynamics in the systems under investigation are described by the Landau-Lifshitz-Gilbert equation:

$$\frac{\partial \mathbf{M}}{\partial t} = -\gamma \mu_0 \mathbf{M} \times \mathbf{H}_{\text{eff}} + \frac{\alpha}{M_S} \mathbf{M} \times \frac{\partial \mathbf{M}}{\partial t}, \tag{1}$$

where $\mathbf{M} = (m_x, m_y, m_z)$ is the magnetization vector, γ is the gyromagnetic ratio, μ_0 is the magnetic permeability of vacuum, and H_{eff} is the effective magnetic field, which is given as follows:

$$\mathbf{H}_{\text{eff}} = H_0 \hat{z} + \frac{2A_{\text{ex}}}{\mu_0 M_S^2} \nabla^2 \mathbf{M} + \frac{2D}{\mu_0 M_S^2} \left(\hat{z} \times \frac{\partial \mathbf{M}}{\partial x} \right) - \nabla \varphi, \tag{2}$$

where A_{ex} is the exchange stiffness constant, D is the IDMI constant, and φ is the magnetic scalar potential fulfilling Maxwell equations in a magnetostatic approximation:

$$\nabla^2 \varphi = \nabla \cdot \mathbf{M}. \tag{3}$$

Equations (1) and (3) are solved numerically in the linear approximation, i.e., assuming $m_x, m_y \ll m_z \approx M_S$, where M_S is saturation magnetization, using the finite-element method in COMSOL Multiphysics environment [29]. Frequency-domain simulations are carried out to calculate the SW dispersion relation in the system of coupled FM layers. Time-domain simulations are performed to demonstrate the functionality of the designed devices. A dynamic magnetic field is used to excite the system sinusoidally at the desired frequency. We use triangular mesh with a maximum element size of 1 nm inside the FM layers and a growth rate of 1.15 outside of the FM layers. We assume that the NM spacer is made from a dielectric material. The metallic layer, such as Cu or Au, can screen the dipolar microwave field [30], causing the reduction of the dipolar interaction between the layers and changing the dispersion relation. However, the effect is negligible for the thin spacer.

In the first step of calculations, we consider a multilayer of the Py(3 nm)/NM(5 nm)/Co(2 nm)/Pt composition. For the Co layer we assume $M_S = 956$ kA/m, exchange stiffness constant $A_{\text{ex}} = 21$ pJ/m [31], Gilbert damping constant $\alpha = 0.05$, IDMI constant $D = -0.7$ mJ/m^2 [32], and for Py layer $M_S = 800$ kA/m, $A_{\text{ex}} = 13$ pJ/m, $\alpha = 0.005$, $D = 0$. External static magnetic field H_0 is fixed to 50 mT.

A. Coupled-mode theory with damping

The SWs propagating in the system composed of two FM layers separated by a NM layer are magnetostatically coupled. We can describe this phenomenon using general coupled-mode theory [33,34] based only on the wave properties. To describe the interaction between propagating modes, we use coupling-in-space formalism. The differential equation describing the scalar wave ψ_l propagating in a single layer l is

$$\frac{d\psi_l}{dx} = -i\beta_l \psi_l, \tag{4}$$

with

$$\beta_l = k_l' - i\alpha_l k_l'' \tag{5}$$

denoting the complex wavevector, where the real part corresponds to the propagation, and the imaginary part to the attenuation of the wave. For the waves propagating in two coupled layers, we get the mutually dependent differential equations:

$$\frac{d\psi_1}{dx} = -i\beta_1 \psi_1 + \kappa_{12} \psi_2, \tag{6}$$

$$\frac{d\psi_2}{dx} = -i\beta_2\psi_2 + \kappa_{21}\psi_1, \tag{7}$$

where for the codirectional coupling, i.e., coupling of the waves propagating in the same direction

$$\kappa_{12} = -\kappa_{21} = \frac{1}{2}\left(|k_P - k_{\mathrm{CP}}| - |k_1 - k_2|\right) \tag{8}$$

are the coupling coefficients. k_P and k_{CP} are wavevectors of the in-phase and in-counterphase modes of the coupled bilayered system, respectively. Generally, the waves can be described by the complex numbers with the coupling magnitude described with the right side of Eq. (8). In our case, we are only interested in the magnitude of coupling, and not the phase of the wave, which derives from the argument of κ_{12}.

The system of differential equations [Eqs. (6) and (7)] can be reduced to the homogeneous linear equations. Assuming that the solutions are in the form of $e^{-i\beta x}$, the solvability condition requires that

$$\beta^2 - (\beta_1 - \beta_2)\beta + (\beta_1\beta_2 + \kappa_{12}\kappa_{21}) = 0. \tag{9}$$

The solutions of this equation are

$$\beta_{\pm} = \bar{\beta} \pm B, \tag{10}$$

where

$$\bar{\beta} = \frac{\beta_1 + \beta_2}{2}, \quad B = \sqrt{\Delta\beta^2 + |\kappa_{12}|^2}, \quad \text{and}$$
$$\Delta\beta = \frac{\beta_1 - \beta_2}{2}.$$

Substituting the solutions of Eq. (10) to Eqs. (6) and (7) and assuming the initial conditions as $\psi_1(0) = A$ and $\psi_2(0) = 0$, we end with the general solutions for the coupled wave functions

$$\psi_1(x) = A\left(\cos Bx - i\frac{\Delta\beta}{B}\sin Bx\right)e^{-i\bar{\beta}x}, \tag{11}$$

$$\psi_2(x) = A\frac{\kappa_{21}}{B}\sin Bx\; e^{-i\bar{\beta}x}. \tag{12}$$

In the synchronous state $k_1' = k_2' = k'$, so we can determine transmission length x_{tr} of the wave from layer 1 to layer 2 [see Fig. 1(b)] from zeroing of the term in the brackets in Eq. (11):

$$x_{\mathrm{tr}} = \frac{1}{B}\left(\frac{\pi}{2} - \arctan\frac{i\Delta\beta}{B}\right). \tag{13}$$

In the synchronous state, $\Delta\beta = -i(\alpha_1 k_1'' - \alpha_2 k_2'')$, so the term in the arctangent is real. In the case when the wave is transferred from the layer with lower damping to the layer with higher damping, the transmission length becomes larger, while in the opposite case, it becomes smaller. If $-\Delta\beta^2 > |\kappa_{12}|^2$, then the parameter B becomes imaginary, and if $\alpha_1 k_1'' < \alpha_2 k_2''$ then $x_{\mathrm{tr}} < 0$ and complete transmission cannot be achieved (the structure behaves like an overdamped harmonic oscillator), while if $\alpha_1 k_1'' > \alpha_2 k_2''$ then $x_{\mathrm{tr}} > 0$ and complete transmission can be achieved but only once.

We can also extract "there and back transmission" length x_{tr2} considering the length at which the wave transfers from layer 1 to layer 2 and then transfers back from layer 2 to layer 1 [see Fig. 1(b)]. The solution comes from zeroing of the sine term in Eq. (12). The lowest positive solution is

$$x_{\mathrm{tr2}} = \frac{\pi}{B}. \tag{14}$$

At this point, we have to introduce the SW parameters to the coupled-mode theory. Knowing that $\omega' = v_{\mathrm{ph}}k'$ and $\omega'' = v_{\mathrm{gr}}k''$ [35], where v_{ph} is the phase velocity and v_{gr} – the group velocity of the SW, Eq. (5) is transformed into

$$\beta_l = \frac{1}{v_{\mathrm{ph},l}}\omega_l' - \frac{i\alpha_l}{v_{\mathrm{gr},l}}\omega_l'', \tag{15}$$

where the real ω' and imaginary ω'' parts of the frequency of a single layer in the Damon-Eshbach geometry are defined as [21,35]

$$\omega' = \gamma\mu_0\left(\sqrt{\left(H_0 + \frac{M_S}{4} + \frac{2A_{\mathrm{ex}}}{\mu_0 M_S}k^2\right)\left(H_0 + \frac{3M_S}{4} + \frac{2A_{\mathrm{ex}}}{\mu_0 M_S}k^2\right) - \frac{e^{-4|k|d}M_S^2}{16}\left(1 + 2e^{2|k|d}\right)} + \frac{2D}{\mu_0 M_S}k\right), \tag{16}$$

$$\omega'' = \gamma\mu_0\left(H_0 + \frac{M_S}{2} + \frac{2A_{\mathrm{ex}}}{\mu_0 M_S}k^2 + \frac{2D}{\mu_0 M_S}k\right). \tag{17}$$

The value of the κ_{12} is determined from the dispersion relation of the coupled bilayer system obtained in the numerical simulations. The parameters in Eq. (8) are calculated for the given frequency ω'.

B. Coupling parameters

To describe the coupling between the SWs propagating in a bilayered structure, we define the two coupling parameters between the FM layers. The first is the power-transfer factor F_P, which relies upon the dispersion relation. From the coupled-mode theory, we get that the power-transfer factor is [34]

$$F_P = \frac{f_{\text{coup}}^2}{f_{\text{coup}}^2 + \Delta f^2}, \tag{18}$$

where

$$\Delta f = |f_1 - f_2|, \quad \text{and} \tag{19}$$

$$f_{\text{coup}} = f_P - f_{\text{CP}} - \Delta f\,, \tag{20}$$

$f_1 = \omega_1/2\pi, f_2 = \omega_2/2\pi$ are frequencies of the SWs in the single layers, f_P and f_{CP} are frequencies of SWs, related to the in-phase and in-counterphase oscillations of the amplitude in the coupled layers, respectively, discussed later in more details.

The second parameter is the energy-distribution factor F_E. We assume that the mode energy of fully coupled SWs is shared equally between both FM layers. The mode energy for uncoupled SWs is accumulated only in one of the layers. The total energy density in the ith layer is

$$E_i = E_{i,\text{dip}} + E_{i,\text{ex}}, \tag{21}$$

where the dipolar-energy density E_{dip} is defined as

$$E_{i,\text{dip}} = \frac{1}{L_i}\frac{1}{2\mu_0}\iint_{S_i} \mathbf{m}\cdot\nabla\varphi\, dy\, dx, \tag{22}$$

and the exchange-energy density E_{ex}

$$E_{i,\text{ex}} = \frac{1}{L_i}\frac{A_{\text{ex}}}{M_S^2}\iint_{S_i} (\nabla\mathbf{m})^2\, dy\, dx, \tag{23}$$

where L_i is the length of the FM layer in the simulations, $S_i = d_i L_i$, where d_i is the thickness of FM layer, and $\mathbf{m} = (m_x, m_y)$ is a dynamical component of the magnetization.

The energy-distribution factor is defined as follows:

$$F_E = 1 - \frac{1}{2}\left|\frac{E_1^P - E_2^P}{E_1^P + E_2^P}\right| - \frac{1}{2}\left|\frac{E_1^{\text{CP}} - E_2^{\text{CP}}}{E_1^{\text{CP}} + E_2^{\text{CP}}}\right|. \tag{24}$$

Values of F_P and F_E are in the range [0,1], where we interpret 0 as no coupling and 1 as a full coupling between SWs propagating in the FM layers.

III. RESULTS

A. Unidirectional coupling in the wide range of frequency

The first step of the investigation of the SW dynamics is the calculation of a dispersion relation. In Fig. 2, we plot the dispersion relations of the Py(3)/NM(5)/Co(2)/Pt multilayer (solid lines) and uncoupled Co(2)/Pt (dashed lines) and Py(3) (dotted lines) layers for two different values of IDMI constant. For $D = 0$ [Fig. 2(a)] all dispersion relations are almost symmetric with respect to $k = 0$ with only small asymmetry related to dipolar interaction. A small change of the dispersion relation for the multilayer, in comparison to the uncoupled layers, is the effect of weak coupling between the FM layers. Taking the nonzero IDMI constant, we introduce strong nonreciprocity to the SW dispersion of the mode related to the Co layer. Interestingly, for $D = -0.7$ mJ/m^2 [see Fig. 2(b)] the dispersion relation for the Co layer almost overlaps with the dispersion relation for Py in the broad range of positive wavevector. Since both modes have almost the same frequency (resonance) and wavevector (phase matching), one can expect strong interaction between them in the multilayer system [34]. Two interacting modes are hybridized forming collective excitations, with in-phase (at frequency f_P) [see inset 3 in Fig. 2(b)] and in-counterphase (at frequency f_{CP}) [see inset 4 in Fig. 2(b)] SW modes at a higher and lower frequency, respectively [29,36]. Indeed, we can see the repulsion of the dispersion branches related to the in-phase and in-counterphase modes for positive k in the multilayer [see the red and blue curves in Fig. 2(b)], being the effect of strong dipolar coupling between modes in Py and Co. For the negative wavevectors, the dispersions for the uncoupled FM layers are well separated, and in the multilayer, they follow the same lines pointing at the weak coupling between FM layers [see insets 1 and 2 in Fig. 2(b)]. Comparing both dispersions in Figs. 2(a) and 2(b), we conclude that adding IDMI to the Co layer can lead to strong SW coupling between FM layers for the waves propagating in one ($+k$) direction, while in the structure without IDMI, the coupling is weak and symmetrical. The general procedure for achieving unidirectional coupling is described in the Appendix.

At this point, we can look at the SW propagation in the Py(3)/NM(5)/Co(2)/Pt multilayer. The model of the investigated structure is shown in Fig. 2(c). The antenna located in the Py layer excites the SW at 15.2-GHz frequency. Over the antenna, we made the indent in the Co/Pt layer to avoid the excitation coming from the dipolar field. It comes from the dispersion relation in Fig. 2(b) that a SW propagating in $+x$ direction should be influenced by the strong coupling between Co and Py layer while propagating in $-x$ direction should go through the Py layer only weakly interacting with the Co layer. Indeed, on the right side

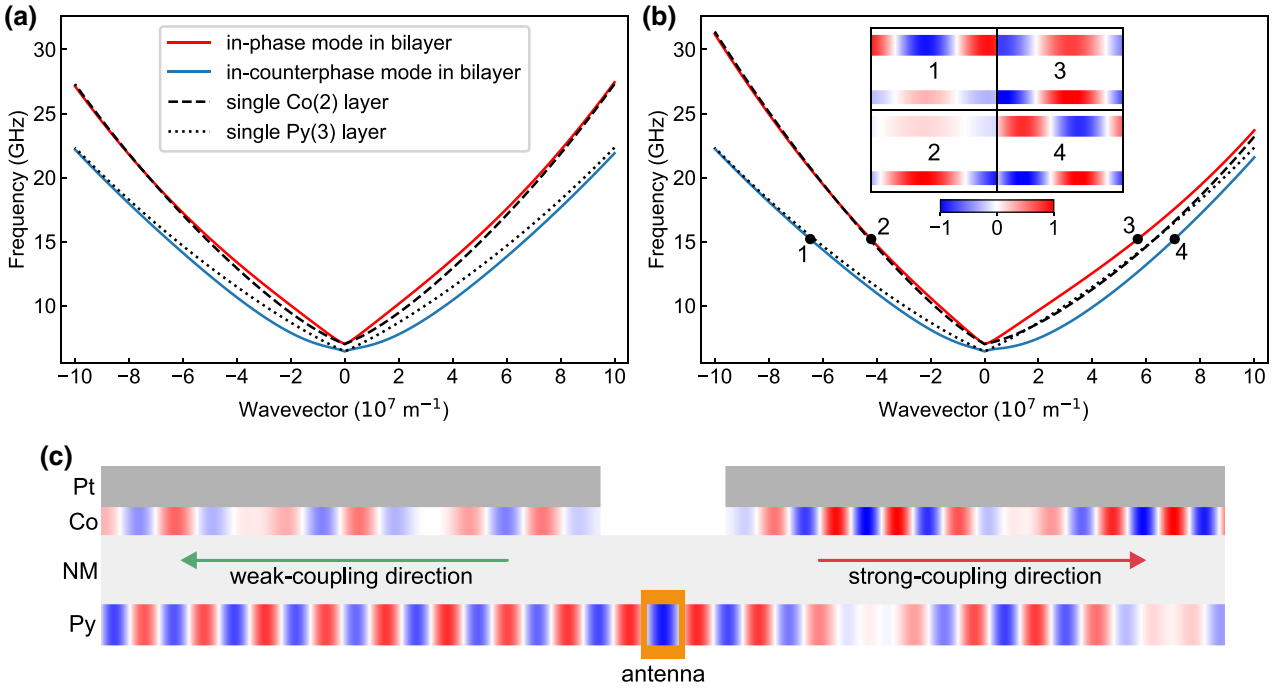

FIG. 2. (a),(b) Dispersion relation of SWs as a function of wavevector k in the Py(3)/NM(5)/Co(2)/Pt multilayer for the IDMI constant in the Co layer (a) $D = 0$ and (b) $D = -0.7$ mJ/m^2. For reference, we show the dispersion relation of SWs in the uncoupled Pt/Co and Py layers with dashed and dotted lines, respectively. In the insets in (b), we show the m_x amplitude of the SWs propagating in both directions at 15.2 GHz. For $D = 0$, the dispersion relation is almost symmetrical with respect to $k = 0$. For $D = -0.7$ mJ/m^2, the IDMI breaks the symmetry leading to strongly coupled modes in the $+k$ range (insets 3 and 4) and single-layer excitation in the $-k$ range (insets 1 and 2). The highest coupling occurs in the region of overlapping of the dispersion relation of the uncoupled layers. (c) Propagation of the SW at 15.2-GHz frequency in the Py(3)/NM(5)/Co(2)/Pt multilayer. The antenna is located in the Py layer, below the indent in the Co/Pt layer. SW propagating in the $+x$ direction transfers back and forth between Py and Co layer. The transmission to the Co layer in the $-x$ direction is weak, and most of the SW intensity remains in the Py layer.

of Fig. 2(c) a SW appears alternately in Co and Py layer being the effect of the interference between in-phase and in-counterphase modes. On the left side, most of the SW intensity remains in the Py layer, with only weak transfer to the Co layer being the effect of weak dynamic coupling. We term this effect as a unidirectional coupling.

For further investigations, the determination of the SW coupling in a broad spectrum is the crucial point. For this purpose, we use the coupling parameters defined in Eqs. (18) and (24). In Fig. 3, we plot F_P (vertical axis) and F_E (color of the points) in the Pt/Co(2)/NM/Py(3) multilayer with $D = -0.7$ mJ/m^2 for different thicknesses of NM layer in dependence on the wavevector of the SW. On the positive k side, both coupling parameters are very close to the maximum value in the range between two dispersion crossing points (1.6×10^7 and 6.3×10^7 m^{-1}). That means the SWs are nearly fully coupled in a wide range of wavevector and frequency. On the negative k side, the coupling is significant only in the long-wavelength range, reaching its maximum for $k \approx -2 \times 10^7$ m^{-1}. The increase of the thickness of the NM spacer leads to a decrease of coupling parameters, except the range of strong coupling between the dispersion crossing points. It is ascribed to the weaker dipolar interaction between the layers.

Another important parameters associated with the coupling between the two layers are the transmission lengths defined in Eqs. (13) and (14). Many parameters affect these physical quantities. We focus on two of them, which are important in our study—the damping constant and the NM-layer thickness. In Fig. 4(a), we show the transmission length in the Py(3)/NM(5)/Co(2)/Pt multilayer depending on the damping constant in the Co layer. In the simulations, the SW source emitting the SW at frequency $\omega'/2\pi = 15.2$ GHz is located in the Py layer. From Eq. (17), we get $\omega''/2\pi = 20.6$ GHz for the Co layer and 19.2 GHz for the Py layer. Results from the numerical simulations are compared with Eqs. (13) and (14) derived from the coupled-mode theory. We get a satisfying agreement between these approaches. Both x_{tr} and x_{tr2} are increasing with the increase of the damping constant. However, x_{tr} is growing faster than x_{tr2} leading to the conclusion that the transmission length from the layer with higher damping (Co layer) to the layer with lower damping (Py layer) is decreasing with the increase of the damping constant. In Fig. 4(b), we show the transmission

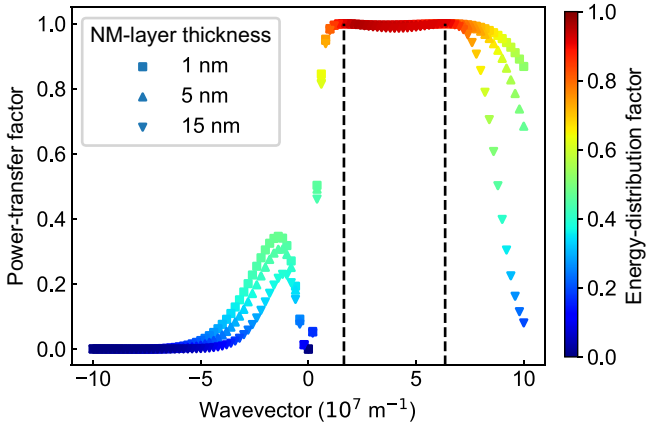

FIG. 3. Power-transfer factor F_P (the vertical axis) and energy-distribution factor F_E (color scale) as a function of the wavevector in the Py(3)/NM(t)/Co(2)/Pt multilayer with the IDMI constant in the Co layer $D = -0.7$ mJ/m^2 for three different thicknesses of the NM layer. We reach coupling parameters close to a maximum value of 1 in the range between 1.6×10^7 and 6.3×10^7 m^{-1} (marked with dashed lines). In the negative k range, the coupling is weak and reduces with the increase of the NM-layer thickness.

length in the Py(3)/NM(t)/Co(2)/Pt multilayer depending on the NM-layer thickness t. We assume $\alpha_{Co} = \alpha_{Py} = 0$. The transmission length is increasing with the exponential character of growth. When $\Delta\beta = 0$, Eq. (13) reduces to the form $x_{tr} = \pi/(2|\kappa_{12}|)$. Thus, the coupling coefficient is decreasing exponentially with the increase of the separation between the layers [37].

B. Spin-wave diode

Taking into account the unidirectional coupling discussed above, we can design the SW diode. The proposed structure is shown in Fig. 5. It consists of continuous Py film, which is the medium where the SWs propagate from the input to the output and Co/Pt stripe, which is a functional element of a diode where IDMI introduces nonreciprocal interaction. They are separated by a 5-nm-thick NM spacer, which is sufficient to neglect Ruderman-Kittel-Kasuya-Yosida interaction. We chose the frequency of the SW from the crossing point of the dispersion relation of uncoupled layers shown in Fig. 2(b) to get the full coupling between FM layers. The width of the Co/Pt stripe is matched to the transmission length x_{tr}, which is related to the coupling strength and the damping in the layers. To determine the efficiency of the device, we calculate the power loss $d_P = 10 \log (E_{in}/E_{out})$, where E_{in} is the energy measured in the steady state in front of the device and E_{out} behind the device, calculated according to Eq. (21).

The operation of the diode is depicted in Figs. 5(a) and 5(b), which shows results from the time-domain simulations of SW continuously excited at the 15.2-GHz frequency in Py at the antenna (A). We fix the width of the

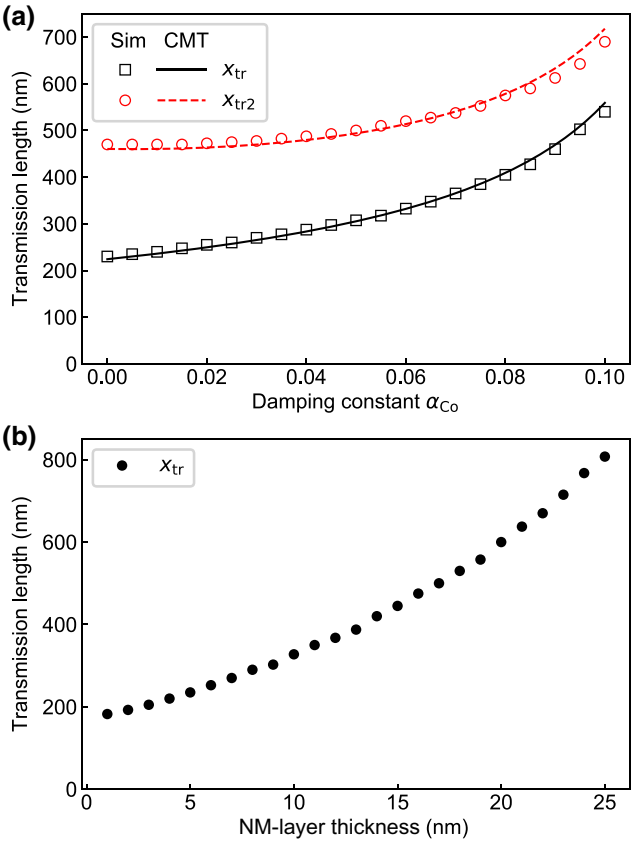

FIG. 4. Transmission-length dependence on (a) the damping constant in the Co layer in the Py(3)/NM(5)/Co(2)/Pt multilayer with the damping in the Py $\alpha_{Py} = 0.005$ and (b) the thickness of NM layer in the Py(3)/NM(t)/Co(2)/Pt multilayer. The source of the SW of 15.2 GHz is located in the Py layer. In (a), the simulations (Sim) results are compared with Eqs. (13) and (14) from the coupled-mode theory (CMT). In (b), we present only the simulation results for x_{tr}.

Co/Pt stripe to 320 nm. The signal for efficiency analysis is collected from the areas marked as input and output ports, which are located at a distance of 20 nm from the Co/Pt stripe edges. Due to weak coupling between the SWs propagating in the $-x$ direction [Fig. 5(a), see also the animation, Movie S1, within the Supplemental Material [38]], the transmission to the Co stripe is small, and the SW passes the diode retaining its intensity. The total power loss in this direction reaches 3.3 dB, and it is mainly due to the Gilbert damping in Py (2.2 dB). On the other hand, the SW propagating in the $+x$ direction [Fig. 5(b), see also the animation, Movie S2, within the Supplemental Material [38]] transfers almost entirely to the Co stripe where it is strongly attenuated due to the high damping. Some residual intensity at the output is the effect of incomplete transfer to Co and return transfer from Co after reflections from the boundaries of the stripe. In fact, along the reverse direction, the total power loss increases to 25 dB. To sum up, the difference in the SW energy in the forward and reverse

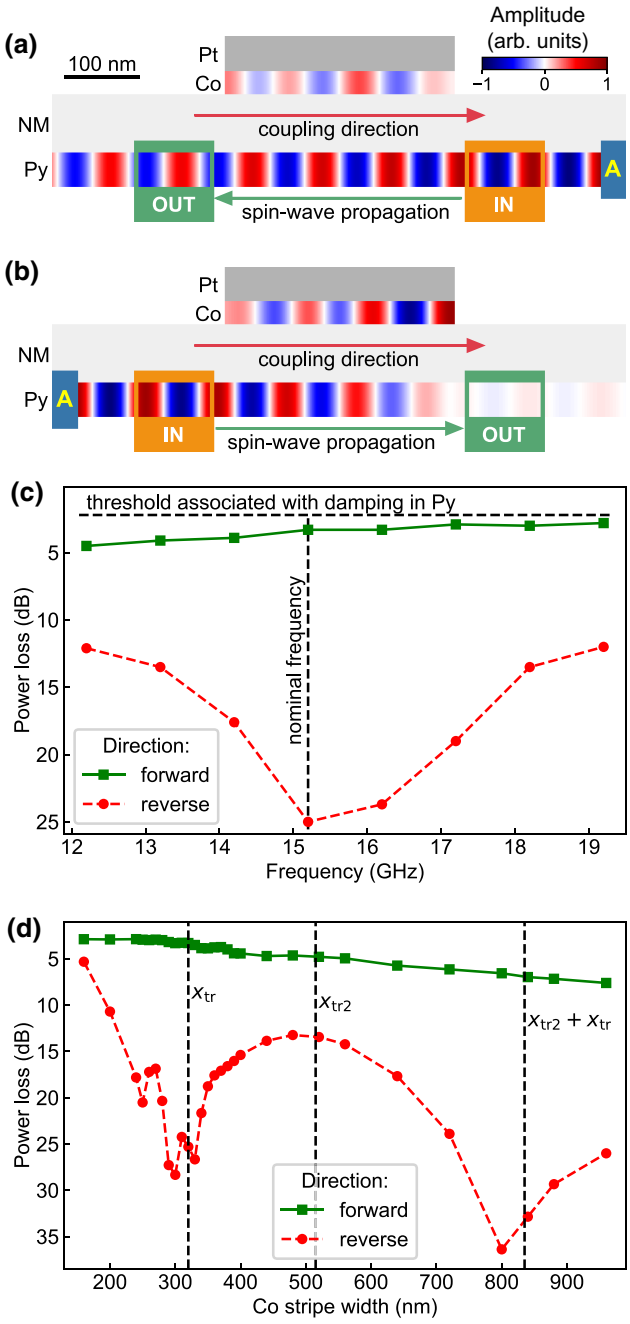

FIG. 5. (a),(b) Propagation of the SW (m_x component) in a diode at 15.2-GHz frequency in Py(3)/NM(5)/Co(2)/Pt in (a) forward and (b) reverse direction for the width of the Co/Pt stripe 320 nm. In (a), the SW propagation direction is opposite to the coupling direction, so that the SW transfers weakly to the Co stripe, and we get a signal of high intensity in the output. In (b), the SW propagation direction is the same as the coupling direction, so that the SW transfers to the Co stripe, where is strongly damped, leading to the low intensity of the signal at the output. (c) The power loss in the forward and reverse direction in dependence on the frequency. In a broad frequency range of 7 GHz, the SW diode preserves its strong isolating properties. (d) The power loss in the forward and reverse direction in dependence on Co stripe width.

direction equals 21.7 dB. The change of the position of the ports impacts the power loss only by the damping in the Py layer, thus it is not changing the difference between the forward and reverse direction.

We investigate the efficiency of the Py(3)/NM(5)/Co(2)/Pt SW diode in the wide range of frequency. Obtained results of the power loss in both directions of propagation are collected in Fig. 5(c). Although SW transmission length varies in dependence on the frequency, the structure preserves strongly asymmetric transmission in a broad range of frequency. In the forward direction, the diode works as well as in nominal frequency. The power loss is decreasing with the frequency due to the decrease of the coupling for negative wavevectors as shown in Fig. 3. The power loss in the reverse direction is reduced but remains significantly higher than in the forward direction. Estimated relative frequency range in which the device works is $\Delta\omega'/\omega_0' \approx 0.5$ (at $\omega_0'/2\pi = 15.2$ GHz).

Additional simulations are made to check the efficiency of the diode for different widths of the Co stripe at 15.2 GHz. The results are presented in Fig. 5(d). The power loss in the forward direction is mainly associated with the damping in the Py layer. A small negative slope reflects the increasing distance between the input and output. In the reverse direction, the most substantial effect on the results come from the SW transmission between the Py and Co layers. The curve reaches the first minimum for 300 nm, being close to $x_{tr} = 320$ nm, then increases up to $x_{tr2} = 515$ nm, and decreases again, reaching the second minimum near $x_{tr2} + x_{tr} = 835$ nm. The power loss in the reverse direction at x_{tr2} is significantly higher than in the forward direction because the SW intensity strongly decreases during the propagation through the Co stripe. Moreover, we perform detailed investigations in the vicinity of x_{tr} in Fig. 5(d) to check if the resonance effect in Co stripe plays any role in the coupling. Indeed, the local maxima and minima in both forward and reverse directions are present with an approximate period of $\lambda/2 = 50$ nm, confirming the influence of the resonance on the power-loss value. However, its impact is small in comparison with the interlayer SW transmission. In conclusion, we show that the SW diode is efficient in a wide range of the Co stripe width.

Moreover, we investigate the SW diode working with SWs of longer (390 nm) wavelength, which should simplify the detection of the effect experimentally. We select another crossing point from Fig. 2(b), located at 8.2-GHz frequency. The width of the Co stripe is set to 190 nm. We obtain a power loss of 6.7 dB in the forward direction and 14.6 dB in the reverse direction. In this case, we distinguish three mechanisms responsible for the smaller efficiency of the diode. First, SWs of longer wavelength are coupled stronger than SWs of shorter wavelength. This effect is shown in Fig. 3. The SW at 8.2 GHz corresponds

to $k = 1.6 \times 10^7$ m^{-1}. The coupling for negative k reaches its maximum in the vicinity of this point. This effect leads to an additional decrease in the signal in the forward direction. Second, the width of the Co stripe is too small to attenuate the SWs in reverse direction effectively. Third, the SW tends to reflect partially inside the Py layer in the points where the Co layer has its boundaries, which leads to additional losses. Besides these limitations, which can be further optimized, the structure is still efficient enough to be considered as a diode.

C. Four-port spin-wave circulator

Next, we exploit the unidirectional coupling further to design a SW circulator. The schematic structure of the four-port circulator is shown in Fig. 6. As compared with the structure of the diode, an additional FM layer is present on the opposite side of the stripe, playing the role of two additional ports. To get the functionality of the circulator, we need the stripe, which is unidirectionally coupled with both top and bottom layers but in opposite directions of SW propagation. We achieve this condition by taking identical outer layers having opposite IDMI constant and the inner stripe lacking IDMI. In our case, we propose to use Py as an IDMI-free coupling stripe and Co/Pt as guiding layers with swapped order in the bottom and top layers. The separation between the stripe and the layer is increased to 15 nm to reduce the dipolar coupling between the Co layers. We keep the width of the Py stripe sufficient to transfer the SW fully from one layer to another, thus for 15.2 GHz, we assume 440 nm. The SW is excited by antenna A, and the SW energy is measured by the ports located 20 nm from the device. Moreover, we perform simulations with assuming no damping to check the efficiency in the ideal case, while the effect of the damping constant is presented further. The structure has a center of symmetry, therefore, the ports on the same diagonal, i.e., P1 and P3 as well as P2 and P4, work identically, and it is sufficient to investigate only two cases—propagation in the coupling and the noncoupling direction.

In the noncoupling case, antenna A is located in the upper-right corner and emits the SWs at 15.2 GHz propagating to the left, as shown in Fig. 6(a) [see also the animation, Movie S3, within the Supplemental Material [38]]. We observe very weak transfer of energy to the Py stripe, so the SW propagates mainly in the top Co layer. The SWs of low intensity in the bottom Co layer result from direct magnetostatic coupling between Co layers. In the lossless structure, the power loss in port P2 reaches 0.2 dB, port P3—12.8 dB, and port P4—19.4 dB. The coupling direction is shown in Fig. 6(b) [see also the animation, Movie S4, within the Supplemental Material [38]]. Here, antenna A is located in the upper-left corner. The SW is transferred to the Py stripe, and it reflects from the right edge of the stripe. After the reflection, the SW is coupled with the bottom Co layer, and, as a result, is transferred to it. In the lossless structure, the power loss in port P3 reaches 0.1 dB, port P4—24.9 dB, and port P1—16.1 dB.

The SW circulator can also be used as a SW diode. However, it benefits the mechanism of the redirection rather than the attenuation of a SW. Considering port P1 and P2 as the input-output ports, the transmission from port P1 to port P2 works as a forward direction and the transmission from port P2 to port P1 as a reverse direction. In that case, the difference in the SW energy in the forward and reverse direction equals 15.9 dB.

Figures 6(c) and 6(d) show the power loss in the circulator as the function of NM-layer thickness for the input port P1 and P2, respectively. We assume $\alpha_{\mathrm{Co}} = \alpha_{\mathrm{Py}} = 0$ to focus on the principle transmission properties of the system. The width of the Py stripe is set to the transmission length, which is plotted in Fig. 4(b). In the noncoupling case [Fig. 6(c)], the power loss in the target port P2 is decreasing, reaching almost no loss for about 10 nm, while in port P3 and P4, we see the oscillations. This is the result of the resonance in the Py stripe. This behavior is even more relevant in Fig. 6(d) representing the coupling case. The power loss in the target port P3 is oscillating in counterphase with respect to port P1. The points with large power loss in port P3 correspond to the width w of the Py stripe fulfilling the resonance condition $w = N\lambda/2$, where $\lambda = 100$ nm. In the resonance, the SW is reflecting from the left side of the Py stripe, and it is coupled with the top Co layer. As a result, we observe the increase of the intensity of the SW in port P1 and, simultaneously, decrease of the intensity in port P3. Interestingly, the effect of negative power loss occurs in Fig. 6(d). It comes from the unwanted effect of the weak direct coupling between Co layers. For the thin NM layer, the coupling is significant enough to reach weak SW transmission from the top to bottom Co layer. In that case, we measure the SW energy in the range where we get the maximum value of the transmission. Moreover, the method of calculating the SW energy does not distinguish between the SW propagating in the left and right direction, which can fix this misleading effect. Moreover, because of the weak direct transmission between Co layers, the power loss can vary depending on the position of the antenna, as well as the position of the ports. However, the effect is relatively small for assumed separation between the outer layers, and the circulator preserves its properties even for ports located far away from the Py stripe edges.

The effect of the damping in the Co layers on the SW circulator functionality is shown in Figs. 6(e) and 6(f). The damping constant in the Py layer is set to 0.005. In the noncoupling direction [Fig. 6(e)], the power loss in port P4 is almost constant, ultimately reaching the value of power loss in target port P2 for $\alpha_{\mathrm{Co}} \approx 0.035$. The mechanism is identical to the one described in Fig. 6(d). The Co layers

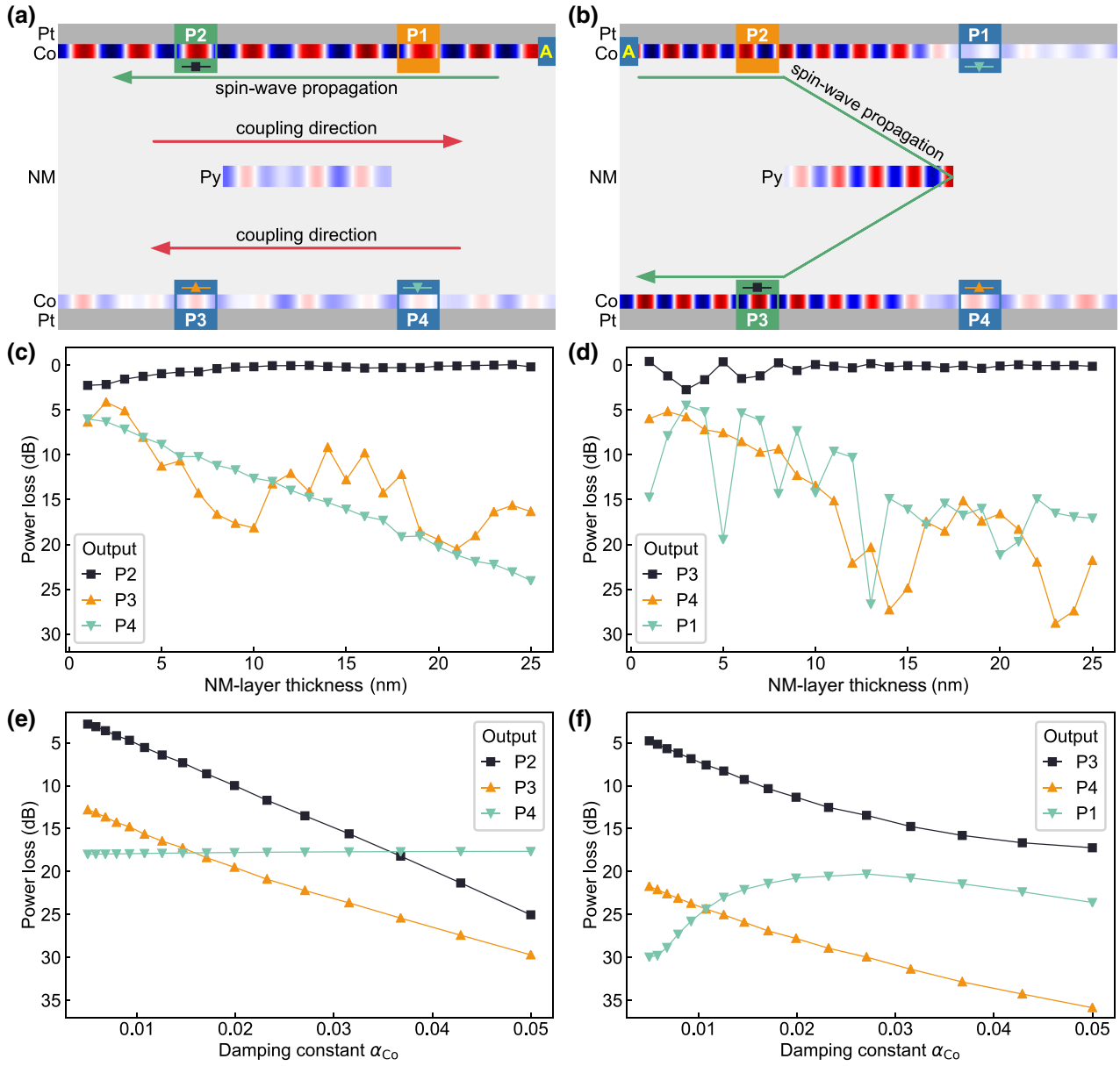

FIG. 6. (a),(b) Model of the four-port SW circulator based on the multilayered structure with unidirectional coupling. Propagation of the SW (m_x component) of 15.2-GHz frequency in the lossless Pt/Co(2)/NM(15)/Py(3)/NM(15)/Co(2)/Pt circulator in the (a) noncoupling direction and (b) coupling direction. In (a), the antenna A is located in the upper-right corner. The SW transfers weakly to the Py layer, so it goes mainly to port P2. In (b), the antenna A is located in the upper-left corner. The SW transfers from the upper Co layer to Py, and after the reflection from the right side of Py, it transfers to the lower Co layer, reaching port P3 in the end. A small-amplitude signal visible at isolated ports is a result of weak direct magnetostatic coupling between Co layers. (c),(d) The power loss measured in the output ports in regard to the input port in dependence on the NM-layer thickness for the input located in (c) port P1 and (d) port P2. In (c), the power loss in the target port P2 is increasing and in the rest of the ports is decreasing with the increase of NM-layer thickness. In (d), the power loss in the target port P3 and port P1 is fluctuating due to the resonance in the Py stripe. The minima of the power loss are corresponding to the Py stripe width fulfilling the resonance condition. (e),(f) The power loss measured in dependence on the damping constant in the Co layer for the input located in (e) port P1 and (f) port P2. In (e), the power loss in port P4 is almost constant, ultimately reaching the value in the target port P2. In (f), the power loss in the target port P2 is significantly larger than in the other ports. The SW circulator is not working properly for $\alpha_{Co} > 0.025$.

are coupled, which leads to the additional SW energy in port P4 coming from the SW going into the circulator. The power loss in port P4 exceeds 35 dB when the SW going into the circulator is excluded from the calculations of the power loss using the reference simulations without the Py stripe. In the coupling direction [Fig. 6(f)], the power loss in port P1 is decreasing with increasing α_{Co} and approaches the value of the power loss in target port P3.

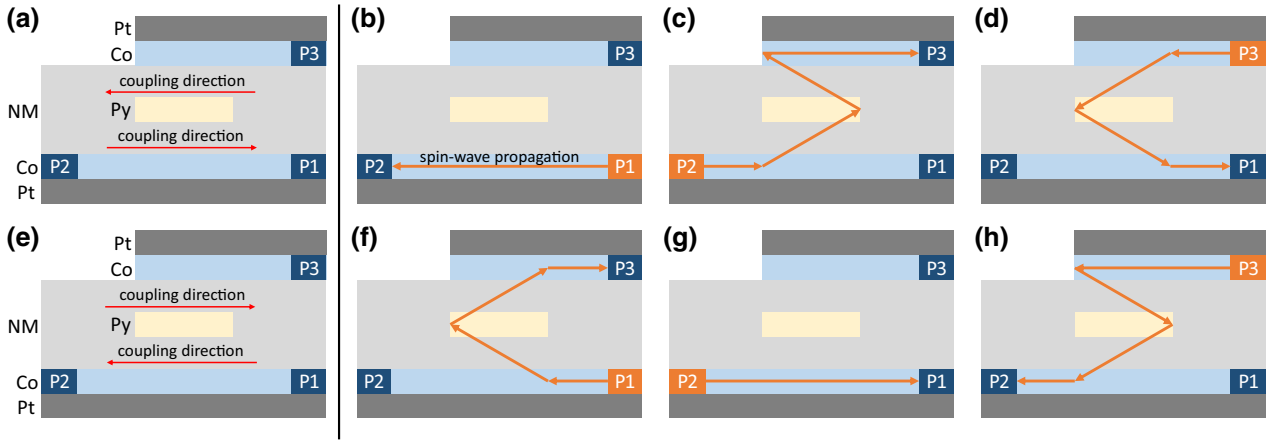

FIG. 7. Three-port SW circulator in (a)–(d) easy-input and (e)–(h) easy-output port P3 configurations. We present the models (a),(e) and the way of acting when the input of SWs is localized in (b),(f) port P1, (c),(g) port P2, and (d),(h) port P3. The coupling direction determines the direction in which the SW will be transmitted from one layer to another. The orange arrows directing from one layer to another denote the SW transmission.

This effect comes from the fact that the SW has to be transmitted from Co to Py as well as from Py to Co. The sign of $\Delta\beta$ in Eq. (13) is opposite for these two cases, and with increasing the difference between the transmission lengths in both directions, the circulator becomes less efficient. In comparison with the SW diode, the damping is, in general, an adverse effect in the SW circulator, so the materials with strong IDMI and low damping are highly desirable. A recent paper indicates Co/Ru as a possible low-damping alternative of Co/Pt bilayers [28,32]. The SW circulator remains efficient for the damping constant $\alpha_{\mathrm{Co}} = 0.017$ reported in Ref. [32].

D. Three-port spin-wave circulator

Along with the four-port circulator, we can propose the three-port circulator with a slightly modified structure, as shown in Fig. 7. As compared to the structure of the four-port circulator, here the upper Co/Pt layer length is reduced and consists now from one port. Furthermore, this layer has to fully cover the Py stripe to preserve the possibility of complete transfer of the SW between the layers. The three-port device does not have any symmetries, therefore, we have to take three cases into account independently. Moreover, the number of cases is doubled due to the reversal of the coupling directions. We can distinguish them by considering the efficiency of port P3 localized in the upper Co layer. If the coupling direction between the upper Co layer and Py stripe is directed onto the port P3, we can consider it as an easy-output port because the SW coming from the Py stripe will be directed straight into port P3 [Fig. 7(f)]. On the other hand, with the opposite coupling direction, the SW coming from port P3 will be transmitted directly to the Py stripe [Fig. 7(d)], and port P3 becomes an easy-input port. Figure 7 shows that the wave propagating from port P2 or P3 in the easy-input or easy-output configuration, respectively, have to reflect two times before reaching the output port [Figs. 7(c) and 7(h)]. On the other hand, in the four-port circulator, only one reflection is needed. It means that the phenomenon in the three-port circulator requires very efficient reflections of SWs from the edges of the stripe. Further investigations are required to optimize its functionality.

IV. CONCLUSIONS

To sum up, we show the effect of unidirectional magnetostatic coupling between the SW modes, which arises due to the IDMI-induced nonreciprocity in the ultrathin multilayer system. The modes related to each layer are strongly coupled in only one direction of the SW propagation in a broad GHz range of frequency. In the opposite direction, within the same range of frequency, the SW modes propagate in only one layer. We propose to exploit this effect for the realization of the magnonic devices in the submicrometer scale. In the Py/NM/Co/Pt structure, limiting the Co/Pt stripe width to the length required to transfer the SW from the Py layer to the stripe, the possibility to get the diode effect is arising. In the forward direction, the SW propagates through the stripe area with small losses associated mainly with the Gilbert damping in Py, while in the reverse direction, the SW transmits to the Co stripe, in which the strong damping significantly reduces the SW intensity in the output. The device works efficiently in a broad range of microwave frequencies, as well as a broad range of Co stripe width. The SW diode can be further improved by opening the possibility to control the magnetization direction in the Co layer and thus becoming the SW transistor [39–45]. The main advantage of the transistor based on the unidirectional coupling is that it will work immediately, so that the time of operation is limited only by the SW velocity and the time needed to reach the steady state.

Another proposed type of the magnonic device, which bases on the same effect, is the SW circulator. It uses the two extended Co layers with Pt inducing IDMI as the waveguides with the input and output ports and the Py stripe in between as a coupler. In each possible case, we get efficient SW transfer to the target port with the strongly suppressed signal at the other ports. The high damping in the Co/Pt films suppresses transmission to the required port of the circulator. To preserve the functionality, the damping constant in the layer shall be smaller than 0.025 and as close as possible to the damping of the Py stripe. In the circulator, the isolation effect in the selected output ports is achieved without involving losses. Moreover, the SW circulator can also work as a diode. A diode and a circulator take a place among the signal processing devices, thus demonstrating unidirectional coupling and proposing magnonic devices open the possibility for further development of energy-efficient, miniaturized beyond-CMOS, magnonic logic components [46–49].

ACKNOWLEDGMENTS

The study has received financial support from the National Science Center of Poland, Projects Nos. UMO-2018/30/Q/ST3/00416 and UMO-2018/28/C/ST3/00052. M.M. acknowledges funding from the Slovak Grant Agency APVV, No. APVV-16-0068 (NanoSky) and APVV-19-0311 (RSWFA). G.G. acknowledges the financial support by the European Metrology Programme for Innovation and Research (EMPIR), under the Grant Agreement 17FUN08 TOPS.

APPENDIX: PROCEDURE FOR ACHIEVING THE UNIDIRECTIONAL COUPLING IN A WIDE FREQUENCY RANGE

The effect of unidirectional coupling of SWs in a wide frequency range can be obtained according to the following procedure. We limit our approach to the Landau-Lifshitz equation consisting of the Zeeman, exchange, magnetostatic, and Dzyaloshinskii-Moriya terms [Eq. (1)].

At first, we assume that the external magnetic field is uniform. Next, one should fulfill a condition, that

$$\text{if } M_{S,\mathrm{FM1}} > (<)\, M_{S,\mathrm{FM2}},$$
$$\text{then } A_{\mathrm{ex,FM1}}/M_{S,\mathrm{FM1}} > (<)\, A_{\mathrm{ex,FM2}}/M_{S,\mathrm{FM2}}.$$

It yields the noncrossing of the dispersion relation between noninteracting bilayers. If this condition is not fulfilled, we always will get crossing of the dispersion relations, and the coupling can be only asymmetric rather than unidirectional. Moreover, it is difficult to obtain the effect of coupling in a wide frequency range without fulfilling this condition. In the last step, the DMI parameter has to be fitted to get proper matching of dispersion relations for noninteracting layers.

[1] M. D. Tocci, M. J. Bloemer, M. Scalora, J. P. Dowling, and C. M. Bowden, Thin-film nonlinear optical diode, Appl. Phys. Lett. **66**, 2324 (1995).
[2] B. Li, L. Wang, and G. Casati, Thermal Diode: Rectification of Heat Flux, Phys. Rev. Lett. **93**, 184301 (2004).
[3] C. W. Chang, D. Okawa, A. Majumdar, and A. Zettl, Solid-state thermal rectifier, Science **314**, 1121 (2006).
[4] B. Liang, B. Yuan, and J.-C. Cheng, Acoustic Diode: Rectification of Acoustic Energy Flux in One-Dimensional Systems, Phys. Rev. Lett. **103**, 104301 (2009).
[5] B. Liang, X. S. Guo, J. Tu, D. Zhang, and J. C. Cheng, An acoustic rectifier, Nat. Mater. **9**, 989 (2010).
[6] S. Borlenghi, W. Wang, H. Fangohr, L. Bergqvist, and A. Delin, Designing a Spin-Seebeck Diode, Phys. Rev. Lett. **112**, 047203 (2014).
[7] J. Wu, X. Yang, S. Beguhn, J. Lou, and N. X. Sun, Nonreciprocal tunable low-loss bandpass filters with ultra-wideband isolation based on magnetostatic surface wave, IEEE Trans. Microw. Theory Techn. **60**, 3959 (2012).
[8] S. Shichi, N. Kanazawa, K. Matsuda, S. Okajima, T. Hasegawa, T. Okada, T. Goto, H. Takagi, and M. Inoue, Spin wave isolator based on frequency displacement nonreciprocity in ferromagnetic bilayer, J. Appl. Phys. **117**, 17D125 (2015).
[9] M. Grassi, M. Geilen, D. Louis, M. Mohseni, T. Brächer, M. Hehn, D. Stoeffler, M. Bailleul, P. Pirro, and Y. Henry, Slow-Wave-Based Nanomagnonic Diode, Phys. Rev. Appl. **14**, 024047 (2020).
[10] J. Lan, W. Yu, R. Wu, and J. Xiao, Spin-Wave Diode, Phys. Rev. X **5**, 041049 (2015).
[11] E. F. Schloemann, Circulators for microwave and millimeter-wave integrated circuits, Proc. IEEE **76**, 188 (1988).
[12] H. Dötsch, N. Bahlmann, O. Zhuromskyy, M. Hammer, L. Wilkens, R. Gerhardt, P. Hertel, and A. F. Popkov, Applications of magneto-optical waveguides in integrated optics: Review, J. Opt. Soc. Am. B **22**, 240 (2005).
[13] V. G. Harris, A. Geiler, Y. Chen, S. D. Yoon, M. Wu, A. Yang, Z. Chen, P. He, P. V. Parimi, X. Zuo, C. E. Patton, M. Abe, O. Acher, and C. Vittoria, Recent advances in processing and applications of microwave ferrites, J. Magn. Magn. Mater. **321**, 2035 (2009).
[14] W. Śmigaj, J. Romero-Vivas, B. Gralak, L. Magdenko, B. Dagens, and M. Vanwolleghem, Magneto-optical circulator designed for operation in a uniform external magnetic field, Opt. Lett. **35**, 568 (2010).
[15] R. Fleury, D. L. Sounas, C. F. Sieck, M. R. Haberman, and A. Alù, Sound isolation and giant linear nonreciprocity in a compact acoustic circulator, Science **343**, 516 (2014).
[16] I. Dzyaloshinsky, A thermodynamic theory of "weak" ferromagnetism of antiferromagnetics, J. Phys. Chem. Solids **4**, 241 (1958).
[17] T. Moriya, Anisotropic superexchange interaction and weak ferromagnetism, Phys. Rev. **120**, 91 (1960).
[18] X. Yu, Y. Onose, N. Kanazawa, J. Park, J. Han, Y. Matsui, N. Nagaosa, and Y. Tokura, Real-space observation of a two-dimensional skyrmion crystal, Nature **465**, 901 (2010).
[19] G. Chen, J. Zhu, A. Quesada, J. Li, A. T. N'Diaye, Y. Huo, T. P. Ma, Y. Chen, H. Y. Kwon, C. Won, Z. Q. Qiu, A. K. Schmid, and Y. Z. Wu, Novel Chiral Magnetic

Domain Wall Structure in Fe/Ni/Cu(001) Films, Phys. Rev. Lett. **110**, 177204 (2013).

[20] L. Udvardi and L. Szunyogh, Chiral Asymmetry of the Spin-Wave Spectra in Ultrathin Magnetic Films, Phys. Rev. Lett. **102**, 207204 (2009).

[21] J.-H. Moon, S.-M. Seo, K.-J. Lee, K.-W. Kim, J. Ryu, H.-W. Lee, R. D. McMichael, and M. D. Stiles, Spin-wave propagation in the presence of interfacial Dzyaloshinskii-Moriya interaction, Phys. Rev. B **88**, 184404 (2013).

[22] D. Cortés-Ortuño and P. Landeros, Influence of the Dzyaloshinskii-Moriya interaction on the spin-wave spectra of thin films, J. Phys.: Condens. Matter **25**, 156001 (2013).

[23] A. A. Stashkevich, M. Belmeguenai, Y. Roussigné, S. M. Cherif, M. Kostylev, M. Gabor, D. Lacour, C. Tiusan, and M. Hehn, Experimental study of spin-wave dispersion in Py/Pt film structures in the presence of an interface Dzyaloshinskii-Moriya interaction, Phys. Rev. B **91**, 214409 (2015).

[24] J. Cho, N.-H. Kim, S. Lee, J.-S. Kim, R. Lavrijsen, A. Solignac, Y. Yin, D.-S. Han, N. J. van Hoof, H. J. Swagten, B. Koopmans, and C.-Y. You, Thickness dependence of the interfacial Dzyaloshinskii-Moriya interaction in inversion symmetry broken systems, Nat. Commun. **6**, 7635 (2015).

[25] M. Garst, J. Waizner, and D. Grundler, Collective spin excitations of helices and magnetic skyrmions: Review and perspectives of magnonics in non-centrosymmetric magnets, J. Phys. D: Appl. Phys. **50**, 293002 (2017).

[26] S. Mühlbauer, B. Binz, F. Jonietz, C. Pfleiderer, A. Rosch, A. Neubauer, R. Georgii, and P. Böni, Skyrmion lattice in a chiral magnet, Science **323**, 915 (2009).

[27] S. Tacchi, R. E. Troncoso, M. Ahlberg, G. Gubbiotti, M. Madami, J. Åkerman, and P. Landeros, Interfacial Dzyaloshinskii-Moriya Interaction in Pt/CoFeB Films: Effect of the Heavy-Metal Thickness, Phys. Rev. Lett. **118**, 147201 (2017).

[28] A. Samardak, A. Kolesnikov, M. Stebliy, L. Chebotkevich, A. Sadovnikov, S. Nikitov, A. Talapatra, J. Mohanty, and A. Ognev, Enhanced interfacial Dzyaloshinskii-Moriya interaction and isolated skyrmions in the inversion-symmetry-broken Ru/Co/W/Ru films, Appl. Phys. Lett. **112**, 192406 (2018).

[29] P. Graczyk, M. Zelent, and M. Krawczyk, Co- and contra-directional vertical coupling between ferromagnetic layers with grating for short-wavelength spin wave generation, New J. Phys. **20**, 053021 (2018).

[30] S. Seshadri, Surface magnetostatic modes of a ferrite slab, Proc. IEEE **58**, 506 (1970).

[31] C. Moreau-Luchaire, C. Moutafis, N. Reyren, J. Sampaio, C. Vaz, N. Van Horne, K. Bouzehouane, K. Garcia, C. Deranlot, P. Warnicke, P. Wohlhüter, J.-M. George, M. Weigand, J. Raabe, V. Cros, and A. Fert, Additive interfacial chiral interaction in multilayers for stabilization of small individual skyrmions at room temperature, Nat. Nanotechnol. **11**, 444 (2016).

[32] T. Ščepka, P. Neilinger, A. Samardak, A. Kolesnikov, A. Ognev, A. Sadovnikov, V. Gubanov, S. Nikitov, K. Palotás, E. Simon, L. Szunyogh, J. Dérer, V. Cambel, and M. Mruczkiewicz, Damping in Ru/Co-based multilayer films with large Dzyaloshinskii-Moriya interaction, arXiv:1911.02467 (2019).

[33] A. Yariv, Coupled-mode theory for guided-wave optics, IEEE J. Quantum Electron. **9**, 919 (1973).

[34] K. Zhang and D. Li, *Electromagnetic Theory for Microwaves and Optoelectronics* (Springer-Verlag, Heidelberg, 2008), 2nd ed.

[35] A. G. Gurevich and G. A. Melkov, *Magnetization Oscillations and Waves* (CRC press, New York, 1996).

[36] M. Mruczkiewicz, M. Krawczyk, V. K. Sakharov, Y. V. Khivintsev, Y. A. Filimonov, and S. A. Nikitov, Standing spin waves in magnonic crystals, J. Appl. Phys. **113**, 093908 (2013).

[37] P. Grünberg, Magnetostatic spin-wave modes of a heterogeneous ferromagnetic double layer, J. Appl. Phys. **52**, 6824 (1981).

[38] See Supplemental Material at http://link.aps.org/supplemental/10.1103/PhysRevApplied.14.034063 for the animations of the SW transmission through the diode and the circulator.

[39] P. Graczyk and M. Krawczyk, Nonresonant amplification of coherent spin waves through voltage-induced interface magnetoelectric effect and spin-transfer torque, arXiv:2001.07474 (2020).

[40] A. I. Nikitchenko and N. A. Pertsev, Spin injection and pumping generated by a direct current flowing through a magnetic tunnel junction, Phys. Rev. B **99**, 224426 (2019).

[41] Z. Duan, C. T. Boone, X. Cheng, I. N. Krivorotov, N. Reckers, S. Stienen, M. Farle, and J. Lindner, Spin-wave modes in permalloy/platinum wires and tuning of the mode damping by spin Hall current, Phys. Rev. B **90**, 024427 (2014).

[42] E. Padrón-Hernández, A. Azevedo, and S. M. Rezende, Amplification of spin waves in yttrium iron garnet films through the spin Hall effect, Appl. Phys. Lett. **99**, 192511 (2011).

[43] A. Khitun, D. E. Nikonov, and K. L. Wang, Magnetoelectric spin wave amplifier for spin wave logic circuits, J. Appl. Phys. **106**, 123909 (2009).

[44] M. Balinskiy, A. C. Chavez, A. Barra, H. Chiang, G. P. Carman, and A. Khitun, Magnetoelectric spin wave modulator based on synthetic multiferroic structure, Sci. Rep. **8**, 10867 (2018).

[45] K. An, D. R. Birt, C.-F. Pai, K. Olsson, D. C. Ralph, R. A. Buhrman, and X. Li, Control of propagating spin waves via spin transfer torque in a metallic bilayer waveguide, Phys. Rev. B **89**, 140405(R) (2014).

[46] Y. Au, M. Dvornik, O. Dmytriiev, and V. Kruglyak, Nanoscale spin wave valve and phase shifter, Appl. Phys. Lett. **100**, 172408 (2012).

[47] A. V. Chumak, A. A. Serga, and B. Hillebrands, Magnon transistor for all-magnon data processing, Nat. Commun. **5**, 4700 (2014).

[48] R. Cheng, M. W. Daniels, J.-G. Zhu, and D. Xiao, Antiferromagnetic spin wave field-effect transistor, Sci. Rep. **6**, 24223 (2016).

[49] J. Cramer, F. Fuhrmann, U. Ritzmann, V. Gall, T. Niizeki, R. Ramos, Z. Qiu, D. Hou, T. Kikkawa, J. Sinova, U. Nowak, E. Saitoh, and M. Kläui, Magnon detection using a ferroic collinear multilayer spin valve, Nat. Commun. **9**, 1089 (2018).